Influence of Permeability on Liquefaction-Induced Shear Deformation

Zhaohui Yang, A.M.ASCE,[1] and Ahmed Elgamal, M.ASCE[2]

Abstract: Permeability of a liquefiable soil profile may affect the rate of pore-pressure buildup and subsequent dissipation during and after earthquake excitation. Consequently, effective soil confinement and available resistance to shear deformations may be significantly dependent on permeability in many practical situations. If present, spatial variation in permeability may even have a more profound impact on available overall shear resistance. Indeed, case histories and experimental evidence (shake table and centrifuge tests) suggest that spatial permeability variation in stratified liquefiable deposits can highly influence the nature and extent of associated lateral deformation. In such situations, the onset of liquefaction-induced densification may result in water or water-rich thin interlayers trapped below overlying low-permeability strata. The presence of these low-shear-strength interlayers may trigger excessive (or even unbounded) localized shear deformations (flow failure mechanism). In this paper, numerical modeling is employed in order to investigate the influence of permeability and the spatial variation thereof on liquefaction-induced shear deformations. The involved response characteristics are numerically simulated using a fully coupled two-phase (solid–fluid) Finite Element program.

Introduction

Liquefaction-induced shear deformation (lateral spreading) continues to be a major cause of earthquake-related damage (Seed et al. 1990; Ishihara et al. 1990, 1992; Bardet et al. 1995; Sitar 1995; Japanese Geotechnical Society 1996, 1998). For sands and silts, the assumption of undrained excess pore-pressure u_e buildup is usually employed for liquefaction susceptibility/triggering analyses (Seed and Idriss 1982; National Research Council 1985; Kramer 1996; Youd and Idriss 1997, 2001). Experimentally, the influence of permeability on liquefaction and associated deformations has been clearly manifested in the results of centrifuge testing investigations (e.g., Tan and Scott 1985; Arulannandan and Scott 1993; Kimura et al. 1998). In such dynamically induced liquefaction studies, scaling laws dictate that prototype permeability be simulated through the use of a higher viscosity pore fluid. Recently, Dewoolkar et al. (1999) conducted a dynamic centrifuge experiment (at a simulated increased gravitational field of 60 g), in which two identical soil profiles were excited simultaneously. The first profile was saturated with water, and the second saturated with a fluid of viscosity 60 times that of water. It was found that higher fluid viscosity (or lower soil permeability coefficient) caused faster buildup and slower dissipation of excess pore pressure. Consequently, in the viscose fluid-saturated soil, liquefaction was reached at all pore-pressure transducer locations, whereas liquefaction was not observed in water-saturated soil.

Spatial variation of permeability in a soil profile is also potentially of primary significance in the development of liquefaction and associated deformations. Early theoretical work on the mechanism of sand boils (Housner 1958, Ambraseys and Sarma 1969; Scott and Zuckerman 1972; National Research Council 1985) attributed the formation of sand boils to inhomogeneity in permeability near the ground surface. Many natural and man-made liquefiable deposits contain stratified sands, and more impervious silts or clays [a typical example is soil strata generated by the hydraulic fill process (Seed 1987)]. During and after earthquake shaking, liquefaction-induced densification may result in a water-rich seam entrapped underneath the relatively impervious materials. Scott and Zuckerman (1972), Liu and Qiao (1984), Elgamal et al. (1989), and Adalier (1992), in small-scale tests of stratified deposits (of varying permeability), observed similar water interlayer formation. In these studies, occurrence of sand boils was also reported. Recently, Kokusho (1999) and Kokusho et al. (1999) conducted one-dimensional (1D) and two-dimensional (2D) liquefaction shaking-table tests to demonstrate the evolution of a water film (trapped below a silt seam), and its key role in dictating the time of occurrence and extent of lateral deformation in sloping ground. In a 2D embankment test, the portion of the embankment above the water interlayer started to slide several seconds after the shaking event, resulting in a (delayed) flow failure.

In view of the potential for a water-interlayer formation underneath an impervious layer, Seed (1987) pointed out the difficulty in obtaining reliable estimates of residual shear strength based on laboratory sample tests. Thereafter, a number of centrifuge model tests were conducted to investigate the effect of permeability variation in liquefiable strata, including Arulanandan et al. (1988), Fiegel and Kutter (1992), Arulanandan and Scott (1993,

[1]Research Fellow, Dept. of Structural Engineering, Univ. of California, San Diego, La Jolla, CA 92093. E-mail: zhyang@ucsd.edu

[2]Professor, Dept. of Structural Engineering, Univ. of California, San Diego, La Jolla, CA 92093 (corresponding author). E-mail: elgamal@ucsd.edu

1994), Zeng and Arulanandan (1995), Balakrishnan et al. (1997), and Balakrishnan and Kutter (1999). Most of these experiments employed clean liquefiable sand profiles overlain by a clay/silt layer.

The above experimental studies were generally motivated by relevant case histories worldwide, such as the Lower San Fernando Dam (Seed et al. 1975, 1989; Davis and Bardet 1996). In the 1978 Izu-Ohshima-Kinkai, Japan Earthquake (Ishihara 1984), one of the Mochikoshi–Tailings–Dam dikes was reported to have failed 24 h after the earthquake (Harder and Stewart 1996). More recently, in the 1994 Northridge, California Earthquake, liquefaction-induced flow failure of the 24-m-high Tapo Canyon Tailings Dam appears to have occurred about 10 min after the main shock (Harder and Stewart 1996). Berrill et al. (1997) and Boukouvalas et al. (1999) also report on delayed flow failures in slopes and bridge foundations.

A number of numerical simulations are presented in this paper to illustrate the characteristics of interaction between permeability and liquefaction-induced shear deformations. These numerical studies were performed using a solid–fluid fully coupled Finite Element program (CYCLIC). The paper first summarizes the key modeling features of CYCLIC, including soil stress–strain (constitutive) model and finite element formulations. Significance of permeability on shear stress–strain response is then illustrated using a single element (for demonstration purposes). Thereafter, numerical studies of permeability effects in both uniform and stratified soil strata are presented and discussed, under conditions of dynamic excitation.

CYCLIC: Finite Element Program for Liquefaction Analysis

In order to study the dynamic response of saturated soil systems as an initial-boundary-value problem, a 2D plane-strain Finite Element (FE) program CYCLIC was developed (Parra 1996; Yang 2000). This program implements the two-phase (solid–fluid) fully coupled FE formulation of Chan (1988) and Zienkiewicz et al. (1990). CYCLIC incorporates a soil constitutive model that was developed for liquefaction analysis (Parra 1996; Yang 2000). In the following sections, the adopted FE formulation and stress–strain model are summarized.

Finite Element Formulation

The saturated soil system is modeled as a two-phase material based on the Biot (1962) theory for porous media. A simplified numerical formulation of this theory, known as $u-p$ formulation in which displacement of the soil skeleton u, and pore pressure p, are the primary unknowns (Chan 1988; Zienkiewicz et al. 1990) was implemented in CYCLIC (Ragheb 1994; Parra 1996; Yang 2000). The computational scheme follows the methodology of Chan (1988), based on the following assumptions: (1) small deformations and negligible rotations, (2) densities of the solid and fluid are constant in both time and space, (3) porosity is locally homogeneous and constant with time, (4) incompressible soil grains, and (5) equal accelerations for the solid and fluid phases.

As described by Chan (1988), the $u-p$ formulation is defined by: (1) an equation of motion for the solid–fluid mixture, and (2) an equation of mass conservation for the mixture, incorporating equation of motion for the fluid phase and Darcy's law

$$\nabla \cdot (\boldsymbol{\sigma}' + p\boldsymbol{\delta}) - \rho(\ddot{\mathbf{u}} - \mathbf{g}) = \mathbf{0} \qquad (1a)$$

$$\nabla \cdot \dot{\mathbf{u}} + \frac{\dot{p}}{Q} + \nabla \cdot \left[\frac{\mathbf{k}}{\rho_f g}(\nabla p - \rho_f \ddot{\mathbf{u}} + \rho_f \mathbf{g})\right] = 0 \qquad (1b)$$
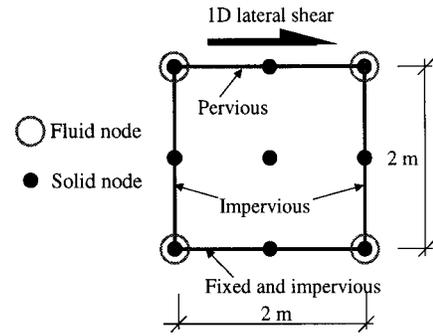

Fig. 1. Typical 9-4-node element employed in solid–fluid coupled formulation, and boundary conditions/applied shear for single element investigation

where $\boldsymbol{\sigma}'$ = effective stress tensor; p = pore-fluid pressure; $\boldsymbol{\delta}$ = second-order identity tensor; ρ = mass density of the mixture; $\mathbf{u}$ = displacement vector of the solid phase; $\mathbf{g}$ = gravity acceleration vector; Q = undrained mixture bulk modulus; $\mathbf{k}$ = Darcy's permeability coefficient tensor; ρ_f = fluid mass density; g = absolute value of gravity acceleration; ∇ = gradient operator; $\nabla \cdot$ = divergence operator; and a superposed dot = material time derivative.

After FE spatial discretization and Galerkin approximation, the governing equations can be expressed in the following matrix form (Chan 1988):

$$\mathbf{M}\ddot{\mathbf{U}} + \int_\Omega \mathbf{B}^T \boldsymbol{\sigma}' \, d\Omega + \mathbf{Q}\mathbf{p} - \mathbf{f}^{\mathbf{s}} = \mathbf{0} \qquad (2a)$$

$$\mathbf{Q}^{\mathbf{T}}\dot{\mathbf{U}} + \mathbf{S}\dot{\mathbf{p}} + \mathbf{H}\mathbf{p} - \mathbf{f}^{\mathbf{p}} = \mathbf{0} \qquad (2b)$$

where $\mathbf{M}$ = mass matrix; $\mathbf{U}$ = displacement vector; $\mathbf{B}$ = strain-displacement matrix; $\boldsymbol{\sigma}'$ = effective stress vector (determined by the soil constitutive model discussed below); $\mathbf{Q}$ = discrete gradient operator coupling the solid and fluid phases; $\mathbf{p}$ = pore pressure vector; $\mathbf{H}$ = permeability matrix; and $\mathbf{S}$ = compressibility matrix. The vectors $\mathbf{f}^{\mathbf{s}}$ and $\mathbf{f}^{\mathbf{p}}$ include the effects of body forces and the prescribed boundary conditions for the solid and fluid phases respectively. In Eq. (2a), the first term represents inertia force of the solid–fluid mixture, followed by internal force due to soil skeleton deformation, and internal force induced by pore-fluid pressure. In Eq. (2b), the first two terms are the rates of volume change with time for the soil skeleton and the fluid phase, respectively, followed by seepage rate of the pore fluid ($\mathbf{H}\mathbf{p}$). It should be noted that a high permeability $\mathbf{k}$ in Eq. (1b) results in a large-valued $\mathbf{H}$ matrix in Eq. (2b), which numerically behaves as a penalty term that forces pore-pressure $\mathbf{p}$ changes to be negligibly small (free drainage scenario).

Eqs. (2a) and (2b) are integrated in time using a single-step predictor multicorrector scheme of the Newmark type (Chan 1988; Parra 1996). The solution is obtained for each time step using the modified Newton–Raphson approach (Parra 1996).

A typical element employed in the $u-p$ formulation is shown in Fig. 1, with nine nodes for the solid phase and four nodes for the fluid phase, so as to reduce numerical difficulties associated with the nearly incompressible fluid phase (Chan 1988). Each solid node is associated with two-degrees-of-freedom (2 DOF) for the lateral and vertical displacements, and each fluid node is associated with 1 DOF for pore pressure. This 9-4-node element is employed in all numerical studies presented herein.
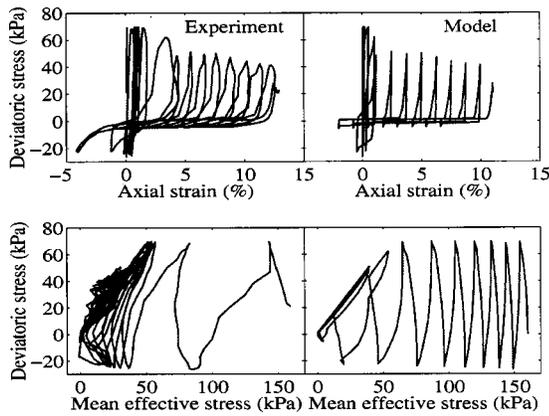
Fig. 2. Recorded and computed results of anisotropically consolidated, undrained cyclic triaxial test (Nevada sand at 40% relative density) with static stress bias (Arulmoli et al. 1992; Yang 2000)

Remarks

1. The permeability coefficient k is a function of void ratio, fluid viscosity, and fluid density (Lambe and Whitman 1969). However, in all the simulations presented in this paper, k for a given material was assumed constant throughout (independent of void ratio change). This simplification is considered reasonable since void ratio change in all cases was less than 10%, with negligible impact on permeability (Lambe and Whitman 1969) and the presented computational results.

2. As mentioned above, the employed FE formulation is based on the small deformation assumption. Generally, this assumption had minimal impact on the presented results and response mechanisms. The relatively large computed simple shear deformations will not be substantially different if estimated by a finite strain formulation.

Constitutive Model

In the developed liquefaction model, emphasis is placed on controlling the magnitude of cycle-by-cycle permanent shear strain accumulation in clean medium-dense sands (Parra 1996; Yang 2000). Specifically, the experimentally observed accumulation of permanent shear strain in Fig. 2 (e.g., Arulmoli et al. 1992) was modeled by using strain-space parameters (Yang 2000), within a multisurface stress-space model (Prevost 1985). Furthermore, appropriate loading–unloading flow rules were devised to reproduce the strong dilation tendency seen in Fig. 2 (Arulmoli et al. 1992), which results in increased cyclic shear stiffness and strength. The main components of this model are summarized below.

Yield Function

Following the classical plasticity convention (Hill 1950), it is assumed that material elasticity is linear and isotropic, and that nonlinearity and anisotropy result from plasticity. The selected yield function (Prevost 1985; Lacy 1986) forms a conical surface in stress space with its apex at $(-p_0')$ along the hydrostatic axis (Fig. 3). In the context of multisurface plasticity (Iwan 1967; Mroz 1967; Prevost 1985), a number of similar yield surfaces with a common apex and different sizes form the hardening zone (Fig. 3). The outmost surface is the envelope of peak shear strength (failure envelope).
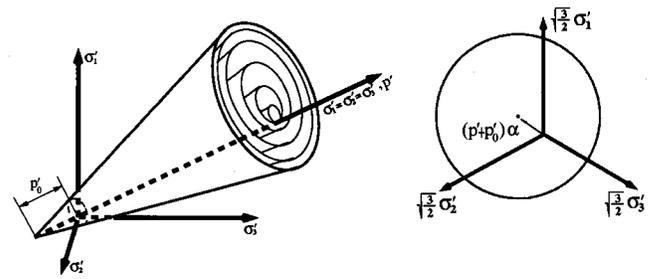

Fig. 3. Conical yield surface in principal stress space and deviatoric plane (after Prevost 1985; Lacy 1986; Parra 1996)

Hardening Rule

A purely deviatoric kinematic hardening rule (Prevost 1985) is employed in order to generate hysteretic response under cyclic shear loading. This kinematic rule dictates that all yield surfaces may translate in stress space within the failure envelope (Hill 1950).

Flow Rule

During shear loading, the soil contractive/dilative behavior is handled by a nonassociative flow rule (Parra 1996) so as to achieve appropriate interaction between shear and volumetric response. In particular, nonassociativity is restricted to the volumetric component P″ of the plastic flow tensor (outer normal to the plastic potential surface in stress space). Therefore, depending on the relative location of the stress state (Fig. 4) with respect to the *phase transformation* (PT) surface (Ishihara 1985; Iai 1991; Vaid and Thomas 1995; Kramer 1996; Dobry and Abdoun 1998; Kramer and Arduino 1999; Vaid and Sivathayalan 1999), different expressions for P″ were specified for (Parra 1996):

1. the contractive phase, when the stress state lies inside the PT surface (Fig. 4, phase 0–1);
2. the dilative phase during loading, if the stress state lies outside the PT surface (Fig. 4, phase 2–3); and
3. the contractive phase during unloading, with the stress state initially outside the PT surface (Fig. 4, phase 3–4).

At low effective confining pressure, when the stress state reaches the PT surface while loading, permanent shear strain may accumulate with essentially no change in shear stress (Fig. 4, phase 1–2). This is achieved by activating a perfectly plastic zone (PPZ)
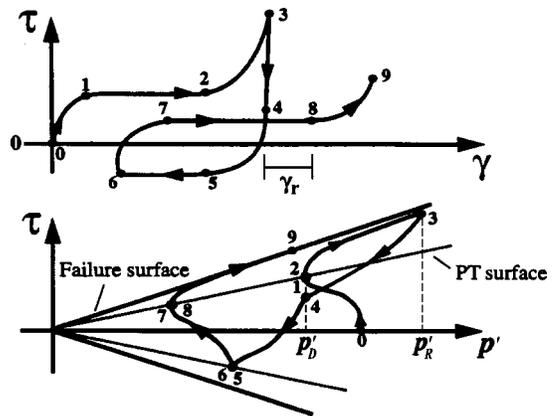

Fig. 4. Schematic of constitutive model response showing octahedral stress τ, effective confinement p', and octahedral strain γ relationship (after Parra 1996)

Table 1. Major Material Properties for Nevada Sand at 40% Relative Density (Arulmoli et al. 1992; Taboada 1995)

Property	Value
Specific gravity	2.68
Saturated unit weight	19.355 kN/m^3
Dry unit weight	15.250 kN/m^3
Minimum void ratio	0.516
Maximum void ratio	0.894
Permeability	6.6×10^{-5} m/s

before the initiation of dilation outside the PT surface (Fig. 4, phase 2–3). The PPZ is defined in deviatoric strain space as a circular, initially isotropic surface (Yang 2000). Depending on the current strain state and plastic loading history, the PPZ may enlarge and/or translate in deviatoric strain space to model the accumulation of permanent shear deformations (Yang 2000).

Limits on Dilation. The dilation rule (Fig. 4, phase 2–3) can result in a significant increase in shear stress and mean effective confining stress. This increase is limited by:
1. Fluid Cavitation (Lambe and Whitman 1969; Casagrande 1975): If soil response is essentially undrained (fluid migration is relatively slow), the tendency for dilation can eventually drop pore pressure to the minimum value of -1.0 atmospheric pressure (i.e., cavitation). Cavitation will prevent the effective confining pressure from further increase.
2. Critical-void-ratio soil response (Casagrande 1936, 1975): If the soil is partially or fully drained (relatively rapid flow of pore fluid), overall volume increase is allowed. To this end, the critical-void-ratio state may be reached, whereupon further shear deformation continues to develop without additional increase in shearing resistance.

Model Calibration

The main modeling parameters include typical dynamic soil properties such as low-strain shear modulus and friction angle, as well as calibration constants to control pore-pressure buildup rate, dilation tendency, and the level of liquefaction-induced cyclic shear strain. The employed model has been extensively calibrated for clean Nevada sand (Table 1) at a relative density of about 40% (Parra 1996; Yang 2000). The calibration phase included results of monotonic and cyclic laboratory tests (Arulmoli et al. 1992, Fig. 2) as well as data from level-ground and mildly inclined infinite-slope dynamic centrifuge-model simulations (Dobry et al. 1995, Taboada 1995). For Nevada sand at about 40% relative density, the stiffness was represented by a low-strain shear modulus of 31.4 MPa at 80 kPa confinement, and the shear strength corresponded to a friction angle of 31°.

In the following numerical studies, this calibrated sand model was employed throughout to represent the dynamic soil properties (with different permeability coefficients). Thus, differences in computed response will be solely due to permeability, in order to highlight its significance. The dynamic soil properties of Nevada sand are therefore implicitly assumed to be representative of a medium-density granular material, with a permeability coefficient in the gravel, sand, or silt range.

Simple Shear Loading in Single Element

A single saturated element (Fig. 1) was used as a simplified environment to demonstrate the influence of permeability on shear
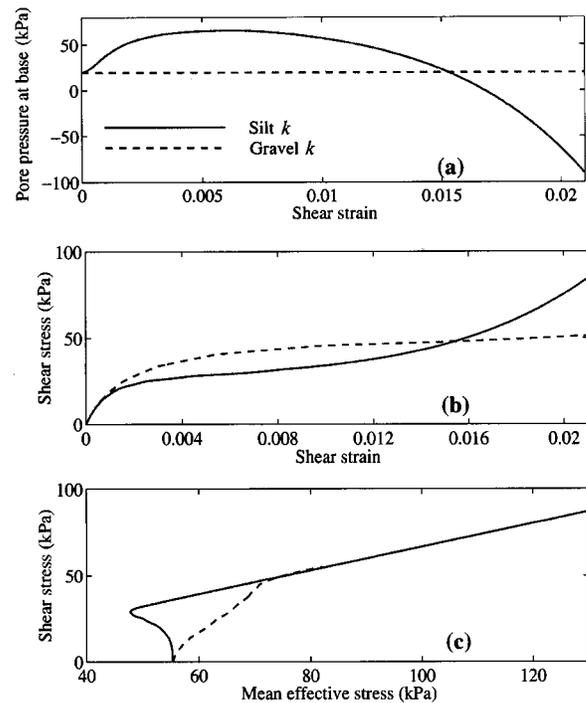

Fig. 5. Pore pressure histories at element base, shear stress–strain, and effective-stress paths at element center

stress–strain response. Two numerical simulations of drained, strain-controlled monotonic 1D lateral shear tests (Fig. 1) were conducted. In the first simulation, a relatively low permeability coefficient k of 6.6×10^{-9} m/s (representative of silt range) was employed. In comparison, a high k of 6.6×10^{-1} m/s (representative of gravel range) was employed in the second simulation. In both cases, the element was initially anisotropically consolidated under a vertical confining pressure of 80 kPa (equivalent of about 8 m of submerged overburden soil pressure). During shear loading, the following boundary conditions were applied to the element (Fig. 1): (1) the base was fixed, (2) the base and two side boundaries were impervious, and (3) the top edge was free draining. Lateral shear strain was applied at a rate of 0.02%/s, to emulate undrained and drained shear response in the silt-k and gravel-k simulations, respectively.

During the shearing process, Fig. 5(a) shows that the silt-k element first experienced a pore-pressure increase (contractive phase), followed by a subsequent reduction (dilative phase). The corresponding shear stress–strain curve [Fig. 5(b)] initially shows a yielding response, followed by a dilation-induced significant regain in stiffness and strength, as the effective-stress path [Fig. 5(c)] approached the failure envelope (above the phase transformation line, see also Fig. 4). In contrast, the gravel-k element shows no change in pore pressure [Fig. 5(a)]. The relatively mild increase in mean effective stress [Fig. 5(c)] is the usual consequence of shear loading in an anisotropic state of soil confinement. Overall, shear-volume interaction had a relatively small effect on the shear stress–strain response [Fig. 5(b)] of this highly permeable element.

The presented numerical simulation (Fig. 5) clearly shows that the silt-k element exhibited a much larger shear resistance compared to the gravel-k element (note that identical mechanical soil properties were employed for the two elements). Soil permeability along with the tendency for dilation at large shear strain is seen to result in this remarkable difference in shearing resistance.
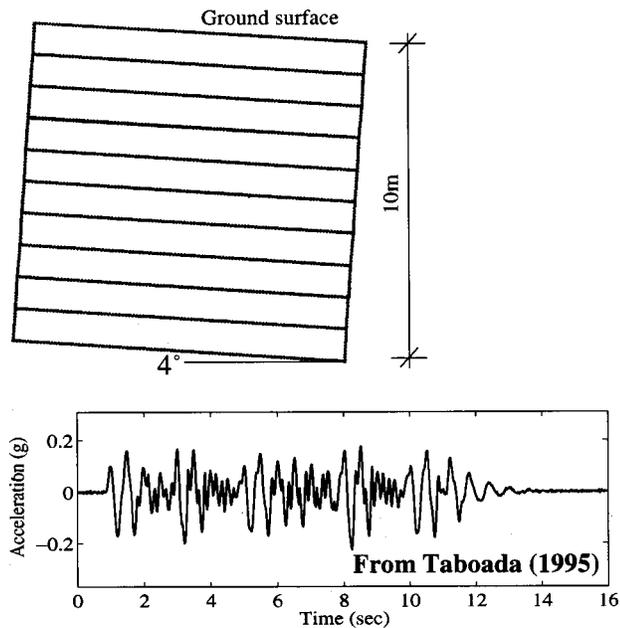
Fig. 6. Employed soil profile and input base acceleration history for uniform-profile simulations

Fig. 7. Lateral displacement histories in uniform soil profile with different permeability coefficients

Dynamic Excitation

Permeability in Uniform Soil Profile

In this section, the influence of permeability in a uniform soil profile composed of a single soil is investigated. A 1D model was employed to represent a 10-m-thick uniform soil profile, inclined by 4° (Fig. 6) to simulate an infinite-slope response. This configuration is identical to that of the VELACS Model-2 centrifuge experiment (Dobry et al. 1995; Taboada 1995), and is modeled using *CYCLIC* by specifying:
1. For the solid phase, the two lateral sides of the mesh were tied together both horizontally and vertically (using the penalty method) to mimic a 1D shear beam effect (Parra 1996), and the top surface was traction free; and
2. For the fluid phase, the base and two sides were impervious, with zero prescribed pore pressure at the ground surface.

The VELACS Model-2 input excitation (harmonic, mainly 2 Hz motion, Fig. 6) was employed in this section. Three numerical simulations were conducted, with a permeability coefficient k of 1.3×10^{-2} m/s (gravel), 3.3×10^{-3} m/s (VELACS Model-2 sandy gravel calibration simulation), and 6.6×10^{-5} m/s (clean sand), respectively.

Computed lateral displacements for the three simulations are displayed in Fig. 7, along with the experimental response of VELACS Model-2 test (Dobry et al. 1995; Taboada 1995). It is clearly seen that (1) computed lateral deformations with the sandy gravel k value are close to the experimental responses (part of the calibration process), and (2) the extent of lateral deformation in this uniform profile is inversely proportional to soil permeability, i.e., a higher k results in smaller lateral deformation (near the surface, the profile with the lowest k value had a lateral translation about 2.5 times that with the highest k values).

The relation between k and deformation is a consequence of the effect of permeability on u_e along the soil profile. Fig. 8 shows that in the case of high k, fast u_e dissipation took place (even during the strong shaking phase), resulting in a low u_e
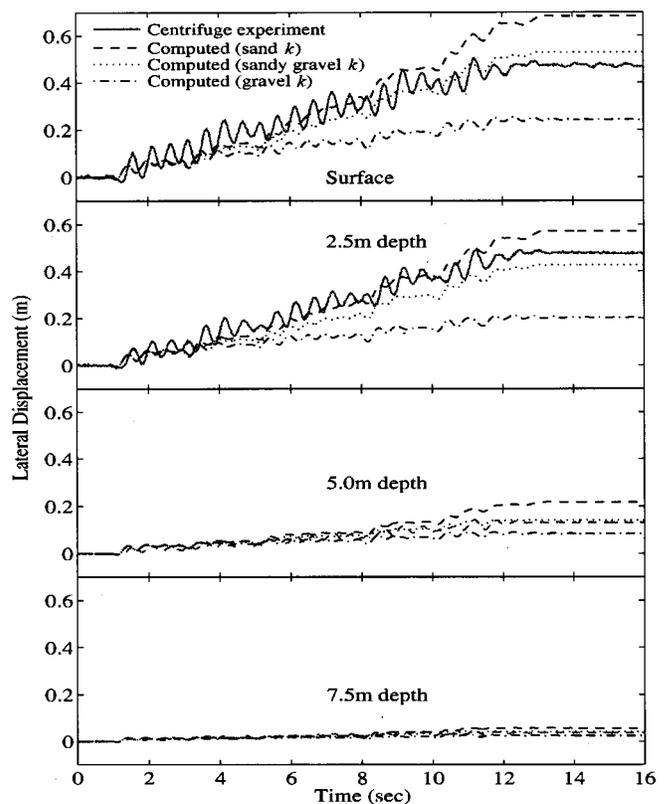
profile. Consequently, high effective confinement was maintained with less reduction in shear stiffness and strength. On the contrary, in the lowest k profile, soil response was essentially undrained, with sustained high u_e long after the shaking phase.

Effect of Low-Permeability Interlayer

As mentioned in the Introduction, shake-table and centrifuge experiments have revealed the importance of low-permeability seams (or interlayers) on the liquefaction-induced response of a cohesionless soil profile. The premise is that a low-shear-resistance (water-rich) interface may develop below the low permeability stratum. Along this low-resistance interface, a flow failure may ensue, with large localized shear strain.

In this section, we attempt to computationally reproduce such a mechanism. Emphasis is placed on the effect of permeability variation on lateral deformation. An inclined (4°) 1D saturated soil profile was employed (Fig. 9). Additional numerical accuracy was achieved through refined modeling of the zone immediately below the low-permeability interlayer as shown in Fig. 9 (details discussed below). Boundary conditions are identical to those of the previous section. Finally, input excitation was defined in the form of 14 cycles of 1 Hz excitation, with an amplitude of 0.08 g (Fig. 9).

Three numerical simulations were conducted, with the permeability coefficient k profiles listed in Table 2. In this table, Case 1 represents a uniform sand stratum throughout (benchmark case), and Cases 2 and 3 include a 0.3 m interlayer of silt k within a uniform sandy-gravel-k stratum (Case 2), and a sand-k stratum (Case 3), respectively. The interlayer profiles were selected to allow for development of a flow failure scenario (due to the in-
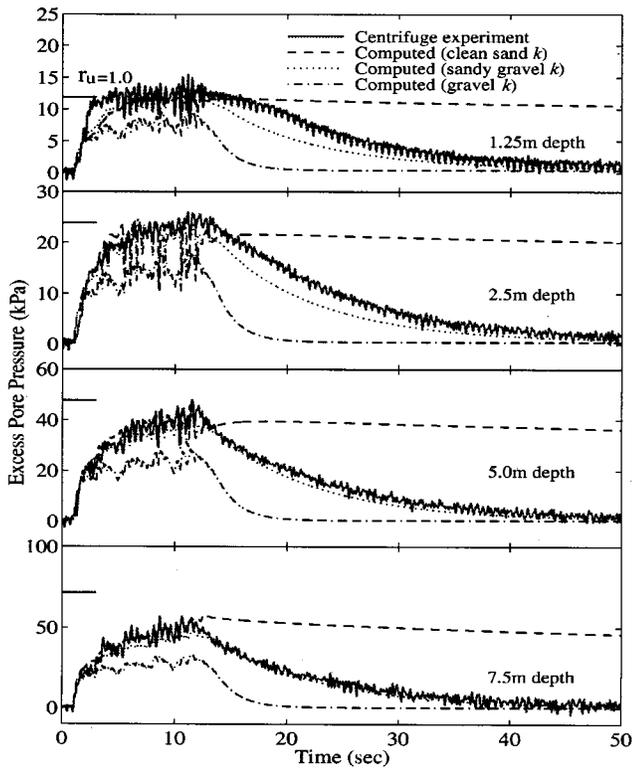
Fig. 8. Excess pore-pressure histories in uniform soil profile with different permeability coefficients (r_u is excess pore pressure ratio $= u_e/\sigma'_v$ where σ'_v is effective vertical stress)

Fig. 9. Employed soil profile and input acceleration history in low-permeability interlayer simulations

terlayer), that initiates during (Case 2), and after (Case 3) dynamic excitation as discussed below.

Fig. 10 depicts the time histories of computed lateral displacement at the surface (location A), immediately below the interlayer (location B), 1.0 m below the interlayer (location C), and 5.0 m below the interlayer (location D). In all cases, displacement stops in the lower sections of the soil column (location C and below) as soon as the shaking ends. The difference in response is in the upper section (location B and above). In Case 1, no further displacement is seen once the shaking stops (similar to the VELACS Model-2 experiment, Fig. 7). In Case 2, the upper section including the silt-k interlayer continues to slide after the shaking ends, in the form of a flow failure. After the shaking phase in Case 3, lateral movement appears to end in the entire column for more than 10 s. Thereafter, a delayed flow-failure scenario occurs.

Flow failure occurred in Case 2 due to the loss of shear strength below the silt-k interlayer. As seen in Fig. 11, this interlayer sustains r_u ($= u_e/\sigma'_v$, where σ'_v is effective vertical stress) at 1.0 (liquefied state) at location B for a long time after the shaking phase. In this illustrative computation, the critical-void-ratio state (selected here at 2% volume increase or about 3.3% void ratio increase) was reached at B before the shaking ended. Hence, the lack of additional dilation and low available shear strength ($r_u = 1.0$) resulted in continued postshaking lateral deformation (flow failure). The detrimental void ratio increase at location B was facilitated by: (1) liquefaction-induced settlement within the sandy-gravel-k stratum below the thin interlayer, and (2) inability of the overlying stratum to match this rate of settlement (due to the low permeability of the interlayer).

In Case 3, the relatively low permeability of the base layer (compared to that of Case 2) resulted in a slower liquefaction-induced settlement rate. At the end of shaking, location B had not
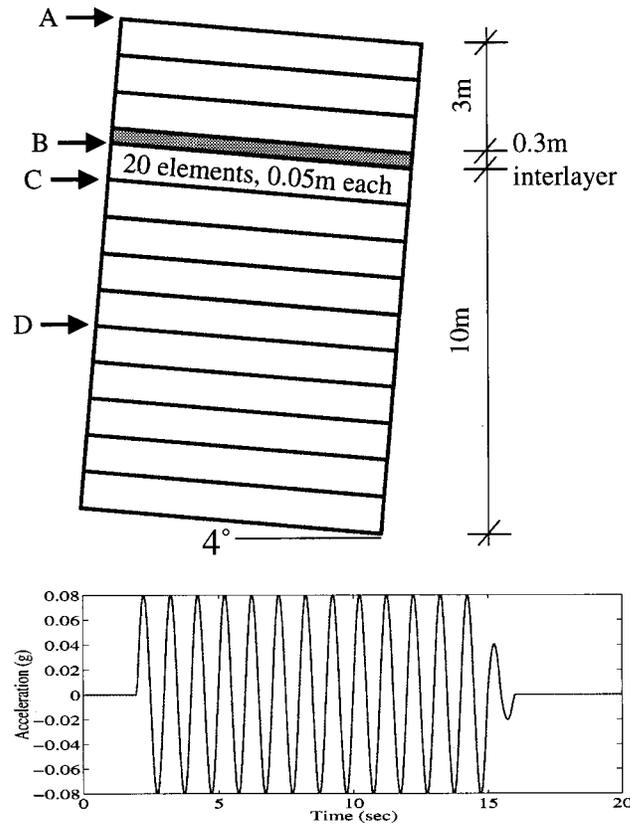
increased in void ratio sufficiently to reach the prescribed critical-void-ratio state. The remaining tendency for dilation resulted in the availability of shear strength to halt further lateral deformation due to the 4° slope inclination. 10 s thereafter, the continued postliquefaction sedimentation (settlement below the thin interlayer) eventually allowed location B to reach the critical-void-ratio state. Thereupon, the lack of dilation tendency and the liquefaction condition ($r_u = 1.0$) resulted in this delayed flow failure situation (Fig. 10). Such delayed flow failure after the end of dynamic/seismic excitation has been reported in the literature by a number of investigators (e.g., Seed 1987; Harder and Stewart 1996, Berrill et al. 1997; Bouckouvalas et al. 1999; Kokusho 1999; Kokusho et al. 1999).

The above discussion is further clarified by the computed shear stress–strain response at location B directly below the silt-k interlayer (Fig. 12). In all three cases, soil strength is seen to gradually decrease, with dilative behavior becoming more pronounced and engaged in resisting the acting dynamic and static shear stresses. In Case 1, after the shaking phase, adequate shear resistance was available to balance the lateral gravity component

Table 2. Permeability Coefficients Employed in Numerical Simulations

Case	Permeability coefficient k (m/s)	
	0.3 m Interlayer	Stratum
1	3.3×10^{-4} (clean sand k)	3.3×10^{-4} (clean sand k)
2	3.3×10^{-8} (silt k)	3.3×10^{-3} (sandy gravel k)
3	3.3×10^{-8} (silt k)	3.3×10^{-4} (clean sand k)
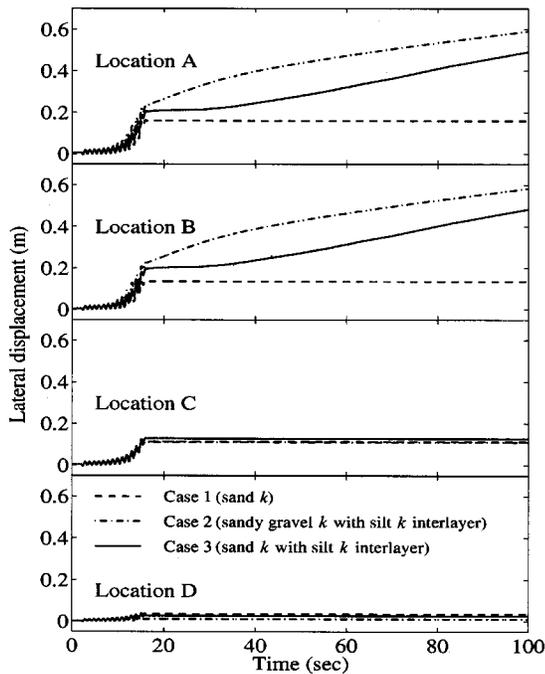
Fig. 10. Lateral displacement histories along soil profile

Fig. 11. Excess pore-pressure histories along soil profile
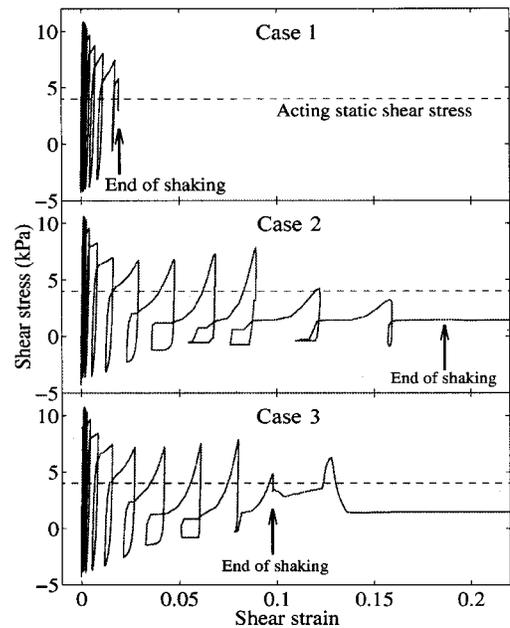
Fig. 12. Shear stress–strain histories directly below interlayer (location B)

of the soil above. In Case 2, soil stiffness and dilatancy effects were completely lost before the end of shaking, and excessive permanent shear strain accumulated after shaking due to insufficient resistance. In Case 3, after the shaking event, a level of shear stress sufficient to maintain equilibrium was present. However, this equilibrium was eventually lost (due to void ratio reaching the critical state), and the soil profile became unstable. Thereafter, excessive permanent shear strain developed (flow failure), in a fashion similar to that of Case 2.
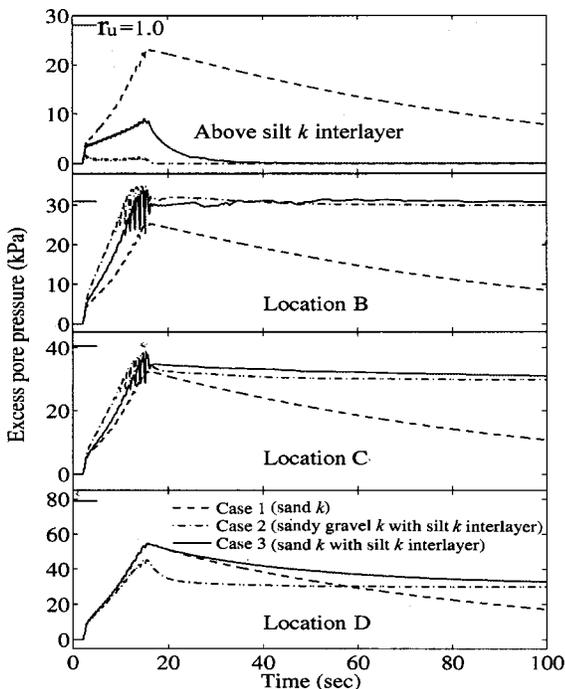
Finally, the influence of a low-permeability interlayer on the overall profile response may be visualized in Figs. 13 and 14, in terms of u_e and deformation profiles along the soil column at 16.5 s (end of shaking) and 80.0 s. In Case 1 (Fig. 13), lateral deformation and u_e profiles were smooth along the soil profile. With no further lateral movement observed during 16.5–80 s, additional vertical settlement continued, as a result of the post-shaking dissipation and the associated reconsolidation processes. In contrast to the above, Fig. 14 (Case 3) with the silt-k interlayer present, shows:

1. A very high pore-pressure gradient within the silt-k layer. Below this layer, the postshaking reconsolidation process eventually results in a constant u_e distribution. This constant value is equal to the initial effective confinement (overbur-
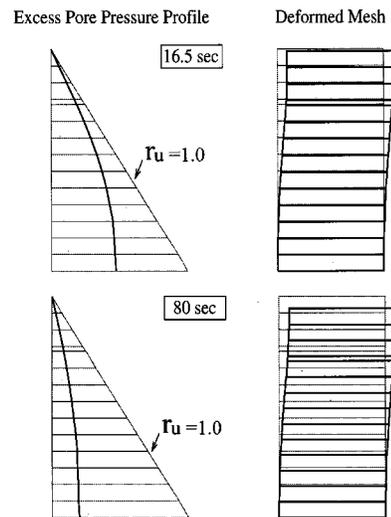

Fig. 13. Excess pore-pressure profile and deformed mesh for case 1: uniform clean sand profile (deformations are not to scale and are exaggerated for clarity)
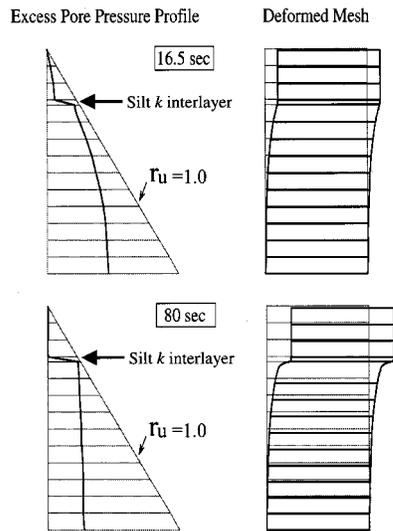
Fig. 14. Excess pore-pressure profile and deformed mesh for case 3: clean sand profile with a silt *k* interlayer (deformations are not to scale and are exaggerated for clarity)

den pressure) imposed by the thin layer and the layers above. Dissipation of this u_e through the low-permeability interlayer may take a very long time in practical situations (if no sand boils develop).

2. After the shaking phase, the void ratio continued to increase immediately beneath the silt-*k* layer (as discussed earlier), with large shear-strain concentration. Meanwhile, negligible additional shear strain was observed in the rest of the profile.

Remarks

In conducting the above computational analyses, it was found that the time needed for location B to reach the critical-void-ratio state depended on element size. The flow-failure state was found to occur earlier as the elements between B and C decreased in size. For an element height of about 0.05 m or less, no further change in the computed results was observed. This issue highlights the significance of high spatial resolution in simulations involving high permeability gradients.

It is also noted that the impervious-interlayer effect may be reduced or minimized in practical situations, due to the prior presence or subsequent development of pervious pathways within this interlayer (possibly leading to the development of sand boils). Therefore, quantification of overall actual (effective) interlayer permeability is a key issue, and should be a topic of much additional research.

Summary and Conclusions

The influence of soil permeability on liquefied soil response was numerically investigated using a two-phase, fully coupled Finite Element program. The framework of this coupled Finite Element formulation and the incorporated liquefaction soil model were summarized. A monotonic shear loading numerical simulation was presented using a single element with a high (gravel) and a low (silt) permeability coefficient (to mimic drained and undrained conditions, respectively). The computational framework was then employed in a 1D mild infinite-slope context to conduct two series of numerical simulations: (1) to document the interaction between soil permeability and the extent of lateral deforma-

tion in a liquefied uniform cohesionless-soil profile, and (2) to illustrate the potential for a lateral deformation flow failure mechanism in liquefiable strata with spatially varying permeability.

In summary, the reported studies aimed to shed light on: (1) the potential significance of permeability in liquefaction-induced shear deformation assessments, (2) the importance of field investigations and research related to quantification of overall site permeability profiles; and (3) the role of relatively impervious narrow seams or interlayers in the possible development of a catastrophic flow failure mechanism. Such situations abound in liquefiable natural (e.g., alluvial) as well as man-made (e.g., hydraulic-fill) soil deposits.

References

Adalier, K. (1992). "Post-liquefaction behavior of soil systems." MS thesis, Rensselaer Polytechnic Institute, Troy, N.Y.

Ambraseys, N., and Sarma, S. (1969). "Liquefaction of soils induced by earthquakes." *Bull. Seismol. Soc. Am.,* 59(2), 651–664.

Arulanandan, K., and Scott, R. F., eds. (1993). "Verification of numerical procedures for the analysis of soil liquefaction problems." *Proc., Conf.,* Balkema, Rotterdam, The Netherlands, Vol. 1.

Arulanandan, K. and Scott, R. F., eds. (1994). "Verification of numerical procedures for the analysis of soil liquefaction problems." *Proc., Conf.,* Balkema, Rotterdam, The Netherlands, Vol. 2.

Arulanandan, K., Yogachandran, C., Muraleetharan, K. K., Kutter, B. L., and Chang, G. S. (1988). "Laboratory flow slide during earthquake simulation." *Proc., Centrifuge 88,* Corte, J.-F., ed., Balkema, Rotterdam, The Netherlands, 539–544.

Arulmoli, K., Muraleetharan, K. K., Hossain, M. M., and Fruth, L. S. (1992). "VELACS: verification of liquefaction analyses by centrifuge studies." *Laboratory Testing Program, Soil Data Rep. No. 90-0562,* The Earth Technology Corporation, Irvine, Calif.

Balakrishnan, A., and Kutter, B. L. (1999). "Settlement, sliding, and liquefaction remediation of layered soil," *J. Geotech. Geoenviron. Eng.,* 125(11), 968–978.

Balakrishnan, A., Kutter, B. L., and Idriss, I. M. (1997). "Liquefaction remediation at bridge sites—centrifuge data report for BAM05." *Rep. No. UCD/CGMDR-97/10,* Center for Geotechnical Modeling, Univ. of California, Davis, Calif.

Bardet, J. P., Oka, F., Sugito, M., and Yashima, A. (1995). "The Great Hanshin Earthquake disaster." *Preliminary Investigation Rep.,* Dept. of Civil Engineering, Univ. of Southern California, Los Angeles.

Berrill, J. B., Christensen, R. J., Keenan, R. J., Okada, W., and Pettinga, J. R. (1997). "Lateral spreading loads on a piled bridge foundation." *Proc., Int. Conf. on Soil Mechanics and Geotechnical Engineering,* Balkema, Rotterdam, The Netherlands, 173–183.

Biot, M. A. (1962). "The mechanics of deformation and acoustic propagation in porous media." *J. Appl. Phys.,* 33(4), 1482–1498.

Bouckovalas, G. D., Gazetas, G., and Papadimitriou, A. G. (1999). "Geotechnical aspects of the 1995 Aegion, Greece, Earthquake." *Proc., 2nd Int. Conf. on Earthquake Geotechnical Engineering,* Balkema, Rotterdam, The Netherlands, 739–748.

Casagrande, A. (1936). "Characteristics of cohesionless soils affecting the stability of earth fills." *J. Boston Soc. Civ. Eng.,* January, 13–33.

Casagrande, A. (1975). "Liquefaction and cyclic deformation of sands—a critical review." *Proc., 5th Pan-American Conf. on Soil Mechanics and Foundation Engineering*, Buenos Aires, Argentina.

Chan, A. H. C. (1988). "A unified finite element solution to static and dynamic problems in geomechanics." PhD dissertation, U. College of Swansea, U.K.

Davis, C. A., and Bardet, J. P. (1996). "Performance of two reservoirs during 1994 Northridge earthquake." *J. Geotech. Eng.,* 122(8), 613–622.

Dewoolkar, M. M., Ko, H.-Y., Stadler, A. T., and Astaneh, S. M. F. (1999). "A substitute pore fluid for seismic centrifuge modeling." *Geotech. Test. J.,* 22(3), 196–210.

Dobry, R., and Abdoun, T. (1998). "Post-triggering response of liquefied sand in the free field and near foundations." *Proc., Geotechnical Earthquake Engineering and Soil Dynamics III*, P. Dakoulas, M. Yegian, and R. D. Holtz. eds., Geotechnical Special Publication No. 75, ASCE, Reston, Va., 270–300.

Dobry, R., Taboada, V., and Liu, L. (1995). "Centrifuge modeling of liquefaction effects during earthquakes." *Keynote Lecture, Proc., 1st Int. Conf. On Earthquake Geotechnical Engineering*, K. Ishihara, ed., Balkema, Rotterdam, The Netherlands, Vol. 3, 1291–1324.

Elgamal, A.-W., Dobry, R., and Adalier, K. (1989). "Study of effects of clay layers on liquefaction of sand deposits using small-scale models." *Proc., 2nd US–Japan Workshop on Liquefaction, Large Ground Deformation and their Effects on Lifelines*, T. D. O'Rourke and M. Hamada, eds., National Center for Earthquake Engineering Research, Buffalo, N.Y. 145–160.

Fiegel, G. L., and Kutter, B. L. (1992). "Liquefaction mechanism for layered soil." *J. Geotech. Eng.,* 120(4), 737–755.

Harder, L. F., and Stewart, J. P. (1996). "Failure of Tapo Canyon Tailings Dam." *J. Perform. Constr. Facil.,* 10(3), 109–114.

Hill, R. (1950). *The mathematical theory of plasticity*, Oxford Univ. Press, London.

Housner, G. W. (1958). "The mechanism of sandblows." *Bull. Seismol. Soc. Am.,* 48(April), 155–161.

Iai, S. (1991). "A strain space multiple mechanism model for cyclic behavior of sand and its application." *Earthquake Engineering Research Rep. No. 43*, Port and Harbor Research Institute, Ministry of Transport, Japan.

Ishihara, K. (1984). "Post-earthquake failure of a tailings dam due to liquefaction of the pond deposit." *Proc., Int. Conf. on Case Histories in Geotechnical Engineering*, Univ. of Missouri-Rolla, St. Louis, 1129–1143.

Ishihara, K. (1985). "Stability of natural deposits during earthquakes." *Theme Lecture, Proc., 11th Int. Conf. on Soil Mechanics and Foundation Engineering*, San Francisco, 321–376.

Ishihara, K., Haeri, S. M., Moinfar, A. A., Towhata, I., and Tsujino, S. (1992). "Geotechnical aspects of the June 20, 1990 Manjil Earthquake in Iran." *Soils Found.,* 32(3), 61–78.

Ishihara, K., Okusa, S., Oyagi, N., and Ischuk, A. (1990). "Liquefaction-induced flow slide in the collapsible loess deposit in soviet tajik." *Soils Found.,* 30(4), 73–89.

Iwan, W. D. (1967). "On a class of models for the yielding behavior of continuous and composite systems." *J. Appl. Mech.,* 34, 612–617.

Japanese Geotechnical Society. (1996). "Special issue on geotechnical aspects of the January 17, 1995 Hyogoken-Nanbu Earthquake." *Soils Found. (Special issue),* 36(1), 1–359.

Japanese Geotechnical Society. (1998). "Special issue on geotechnical aspects of the January 17, 1995 Hyogoken–Nanbu Earthquake, No. 2." *Soils Found. (Special issue),* 38(2), 1–216.

Kimura, T., Kusakabe, O., and Takemura, J., eds. (1998). "Centrifuge 98." *Proc., Int. Conf. Centrifuge 98*, Balkema, Rotterdam, The Netherlands, Vol. 1.

Kokusho, T. (1999). "Water film in liquefied sand and its effect on lateral spread." *J. Geotech. Geoenviron. Eng.,* 125(10), 817–826.

Kokusho, T., Kojima, T., and Nonaka, N. (1999). "Emergence of water film in liquefied sand and its role in lateral flow." *Proc., 12th World Conf. on Earthquake Engineering*, (CD-Rom), Auckland, New Zealand.

Kramer, S. L. (1996). *Geotechnical earthquake engineering*, Prentice–Hall, Upper Saddle River, N.J.

Kramer, S., and Arduino, P. (1999). "Constitutive modeling of cyclic mobility and implications for site response." *Proc., 2nd Int. Conf. on Earthquake Geotechnical Engineering*, Balkema, Rotterdam, The Netherlands, 1029–1034.

Lacy, S. (1986). "Numerical procedures for nonlinear transient analysis of two-phase soil system." PhD dissertation, Princeton Univ., Princeton, N.J.

Lambe, T. W., and Whitman, R. V. (1969). *Soil mechanics*, Wiley, New York.

Liu, H., and Qiao, T. (1984). "Liquefaction potential of saturated sand deposits underlying foundation of structure." *Proc., 8th World Conf. on Earthquake Engineering*, San Francisco, 199–206.

Mroz, Z. (1967). "On the description of anisotropic work hardening." *J. Mech. Phys. Solids,* 15, 163–175.

National Research Council (1985). "Liquefaction of soils during earthquakes." *Rep. by the Committee on Earthquake Engineering*, National Research Council, National Academy Press.

Parra, E. (1996). "Numerical modeling of liquefaction and lateral ground deformation including cyclic mobility and dilation response in soil systems." PhD thesis, Rensselaer Polytechnic Institute, Troy, N.Y.

Prevost, J. H. (1985). "A simple plasticity theory for frictional cohesionless soils." *Soil Dyn. Earthquake Eng.,* 4(1), 9–17.

Ragheb, A. (1994). "Numerical analysis of seismically induced deformations in saturated granular soil strata." PhD thesis, Rensselaer Polytechnic Institute, Troy, N.Y.

Scott, R. F., and Zuckerman, K. A. (1972). "Sandblows and liquefaction." *The great Alaska earthquake of 1964-engineering publication 1606*, National Academy of Sciences, Washington, D.C., 179–189.

Seed, H. B. (1987). "Design problems in soil liquefaction." *J. Geotech. Eng.,* 113(8), 827–845.

Seed, R. B., Dickenson, S. E., Riemer, M. F., Bray, J. D., Sitar, N., Mitchell, J. K., Idriss, I. M., Kayen, R. E., Kropp, A., Hander, L. F. Jr., and Power, M. S. (1990). "Preliminary report on the principal geotechnical aspects of the October 17, 1989, Loma Prieta Earthquake." *Rep. No. UCB/EERC-90/05*, Earthquake Engineering Research Center, Univ. of California, Berkeley, Calif.

Seed, H. B., and Idriss, I. M. (1982). "Ground motions and soil liquefaction during earthquakes." *Earthquake Engineering Research Center Monograph*, EERI, Berkeley, Calif.

Seed, H. B., Lee, K. L., Idriss, I. M., and Makdisi, F. I. (1975). "The slides on the San Fernando Dams during the earthquake of February 9, 1971." *J. Geotech. Eng. Div., Am. Soc. Civ. Eng.,* 101(7), 651–688.

Seed, H. B., Seed, R. B., Harder, L. F., and Jong, H. L. (1989). "Reevaluation of the slide in the Lower San Fernando Dam in the 1971 San Fernando earthquake." *Rep. No. UCB/EERC-88/04,* Univ. of California, Berkeley, Calif.

Sitar, N., ed. (1995). "Geotechnical reconnaissance of the effects of the January 17, 1995, Hyogoken-Nanbu Earthquake Japan." *Rep. No. UCB/EERC-95/01*, Earthquake Engineering Research Center, Univ. of California, Berkeley, Calif.

Taboada, V. M. (1995). "Centrifuge modeling of earthquake-induced lateral spreading in sand using a laminar box." PhD thesis, Rensselaer Polytechnic Institute, Troy, N.Y.

Tan, T. S., and Scott, R. F. (1985). "Centrifuge scaling considerations for fluid-particle systems." *Geotechnique,* 35(4), 461–470.

Vaid, Y. P., and Sivathayalan, S. (1999). "Fundamental factors affecting liquefaction susceptibility of sands." *Physics and mechanics of soil liquefaction*, P. Lade and J. Yamamuro, eds., Balkema, Rotterdam, The Netherlands, 105–120.

Vaid, Y. P., and Thomas, J. (1995). "Liquefaction and postliquefaction behavior of sand." *J. Geotech. Eng.,* 121(2), 163–173.

Yang, Z. (2000). "Numerical modeling of earthquake site response including dilation and liquefaction." PhD dissertation, Columbia Univ., New York.

Youd, T. L., and Idriss, I. M. (1997). "Proceedings of the NCEER work-

shop on evaluation of liquefaction resistance of soils.'' *Rep. No. NCEER 97-0022*, National Center for Earthquake Engineering Research, Buffalo, N.Y.

Youd, T. L., and Idriss, I. M. (2001). ''Liquefaction resistance of soils: summary report from the 1996 NCEER and 1998 NCEER/NSF workshops on evaluation of liquefaction resistance of soils.'' *J. Geotech. Geoenviron. Eng.,* 127(4), 297–313.

Zeng, X., and Arulanandan, K. (1995). ''Modeling lateral sliding of slope due to liquefaction of sand layer.'' *J. Geotech. Eng.,* 121(11), 814–816.

Zienkiewicz, O. C., Chan, A. H. C., Pastor, M., Paul, D. K., and Shiomi, T. (1990). ''Static and dynamic behavior of soils: a rational approach to quantitative solutions: I. fully saturated problems.'' *Proc. R. Soc. London, Ser. A,* 429, 285–309.